Optimization of 3D controlled ELM-free state with recovered global confinement for KSTAR with n=1 resonant magnetic field perturbation

S.K.Kim,[1] R.Shousha,[1] S.H.Hahn,[2] A.O.Nelson,[1,3] J.Wai,[1] S.M.Yang,[4] J.-K.Park,[4] R.Nazikian,[4] N.C.Logan,[5] Y.M.Jeon,[2] Y.In,[6] J.H.Lee,[2] J.Kim,[2] C.Y. Lee,[7] Y.-S. Na,[7] and E.Kolemen[1,4]

[1)] *Princeton University*

[2)] *Korea Institute of Fusion Energy*

[3)] *Columbia University*

[4)] *Princeton Plasma Physics Laboratory*

[5)] *Lawrence Livermore National Laboratory*

[6)] *Ulsan National Institute of Science Technology*

[7)] *Seoul National University*

(Dated: 11 December 2021)

Mitigation of deleterious heat flux from edge-localized modes (ELMs) on fusion reactors is often attempted with 3D perturbations of the confining magnetic fields. However, the established technique of resonant magnetic perturbations (RMPs) also degrades plasma performance, complicating implementation on future fusion reactors. In this paper, we introduce an adaptive real-time control scheme on the KSTAR tokamak as a viable approach to achieve an ELM-free state and simultaneously recover high-confinement ($\beta_N \sim 1.91$, $\beta_p \sim 1.53$, and $H_{98} \sim 0.9$), demonstrating successful handling of a volatile complex system through adaptive measures. We show that, by exploiting a salient hysteresis process to adaptively minimize the RMP strength, stable ELM suppression can be achieved while actively encouraging confinement recovery. This is made possible by a self-organized transport response in the plasma edge which reinforces the confinement improvement through a widening of the ion temperature pedestal and promotes control stability, in contrast to the deteriorating effect on performance observed in standard RMP experiments. These results establish the real-time approach as an up-and-coming solution towards an optimized ELM-free state, which is an important step for the operation of ITER and reactor-grade tokamak plasmas.

I. INTRODUCTION

When sufficiently heated, magnetically confined tokamak plasmas spontaneously transition to a high confinement mode (H-mode)[1] - a promising plasma operation scenario for future fusion power plants. The H-mode is characterized by a narrow edge transport barrier concomitant with the formation of an edge pedestal with a steep pressure gradient. This “pedestal" not only enhances performance in the core region but also increases the non-inductive current, improving the fusion economy by reducing the external heating and recirculating power required for steady-state operation. Because of these advantages, the ITER baseline scenario[2] plans to utilize H-mode plasmas to demonstrate burning plasma in a tokamak for the first time. However, H-mode also presents serious risks to reactor operation, most prominently through the creation of dangerous edge instabilities called edge localized modes (ELMs)[3]. These rapid relaxations of the pedestal density and temperature result in intense transient heat fluxes on the reactor walls, leading to undesired material erosion and surface melting which will not be acceptable in a reactor scenario[4,5]. Therefore, to retain the tokamak design as a viable option for fusion reactors, it is critical that we develop methods to routinely suppress ELM events without degrading the plasma performance.

One of the most effective methods to control ELMs is to apply resonant magnetic perturbations (RMPs) using 3D coils[6–9]. RMPs suppress ELMs by causing additional transport[10–23] in the pedestal, degrading its height to a point where ELMs are no longer unstable[24–26]. However, this inevitably comes at the considerable expense of global confinement deterioration, decreased access to high-performance plasma regimes and thus depleted economic prospects. This degradation tends to be greater with a lower toroidal wave number (n) of RMP. Even so, the use of low-n configurations will be important at the reactor level due to the strong decay of external fields in the thick shielding between the plasma and field coils. Undoubtedly, the compatibility of RMP ELM suppression with high confinement operation requires urgent exploration.

In this context, we report on an adaptive RMP scheme capable of maximizing plasma performance while maintaining robust ELM suppression. With this new technique, up to $\sim 70\%$ of the RMP-induced performance degradation can be quickly recovered, returning the plasma to a high-power state suitable for future reactors. By exploiting a salient hysteresis process on the KSTAR tokamak[27], we find that RMP-induced transport does not just produce a negative influence on confinement (as is typically assumed) but instead also opens up a pathway to strong recovery of plasma performance that is accessible to a highly-optimized controller. This leads to the concur-

rent establishment of high confinement plasmas and sustained ELM suppression at normalized performance close to the ITER-baseline level, reaching $\beta_N \sim 1.91$, $\beta_p \sim 1.53$, and $H_{98} \sim 0.9$. Here, $\beta_N = \frac{aB_T}{I_p}\frac{p}{B^2/2\mu_0}$ is the normalized beta, $\beta_p = \frac{p}{B_p^2/2\mu_0}$ is the poloidal beta, and $H_{98} = \tau_{exp}/\tau_{98}$ is the thermal energy confinement quality compared to the standard H-mode plasmas, where p is the averaged plasma pressure, a is the minor radius, I_p is the total plasma current, B_T is the toroidal magnetic field, B_p is the poloidal magnetic field, B is the total magnetic field, τ_{exp} is the experimental thermal energy confinement time, and τ_{98} is the empirically derived confinement time using standard H-mode database[28]. Since H_{98} enters to the power of 3.23 in determining the fusion gain Q_{fus}[29], where Q_{fus} is the ratio between produced fusion energy over input, the strong recovery of H_{98} demonstrated in this work allows a substantial reduction of fusion cost, establishing a means with which RMPs can be used for ELM suppression to enable commercial-grade fusion devices.

In this paper, the descriptions of the adaptive scheme and experimental results are given in section 1. Section 2 describes its advantage in terms of achieving safe ELM suppression by avoiding mode locking. In sections 3, the widened ion temperature pedestal during ELM-free state and its effect on the performance recovery are presented, respectively. A possible mechanism of ion temperature pedestal widening is also discussed in following section. Lastly, conclusions are drawn in section 5.

II. OPTIMIZED ELM-FREE STATE BY ADAPTIVE SCHEME

A. ELM suppression using adaptive RMP amplitude control

The real-time adaptive approach in this study detects ELMs from a D_α emission measurement and finds the optimum RMP strength or coil current I_{RMP} sufficient to maintain the ELM-free state while small enough to maximize the confinement. The adaptive ELM control experiment (#26004) in KSTAR introduced here is outlined in Fig.1. Figure.1 shows a H-mode plasma with fully suppressed ELMs via adaptive feedback RMP amplitude control. The relevant plasma parameters are plasma major radius $R_0 = 1.8$ m, minor radius $a_0 = 0.45$ m, the toroidal magnetic field $B_T = 1.8 - 2.3$ T at major radius R_0, Greenwald density fraction $n_G \sim 0.4$, elongation $\kappa \sim 1.71$, upper triangularity $\delta_{up} \sim 0.37$, lower triangularity $\delta_{low} \sim 0.85$, and pedestal collisionality $\nu_{e,ped}$ 0.5. In this discharge, a hysteresis effect is utilized where ELM suppression can be maintained over

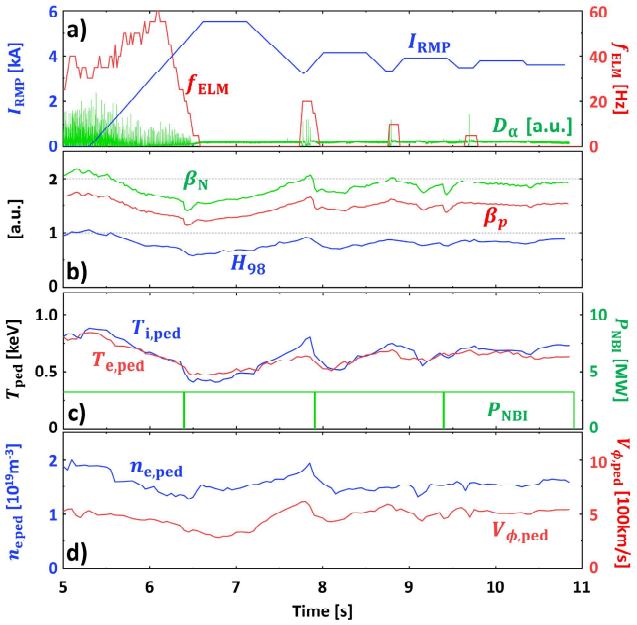

FIG. 1. Time traces of discharge #26004 with adaptive ELM control using n = 1 RMP (#26004) with adaptive RMP control. **a** RMP coil current I_{RMP} (blue), D_α emission (green) near outer divertor target, and detected ELM frequency f_{ELM} (red). **b** Plasma confinement scaling H_{98}(blue), normalized beta β_{N} (green), and poloidal beta β_{p} (red). **c** Pedestal height of ion $T_{\mathrm{i,ped}}$ (red), electron $T_{\mathrm{e,ped}}$ (blue) temperature, and NBI heating power P_{NBI} (green). **d** Pedestal height of electron density $n_{\mathrm{e,ped}}$ (blue) and toroidal rotation $V_{\phi,\mathrm{ped}}$ of carbon (6+) impurity in co-I_{p} direction (red).

long periods with a lower RMP strength than initially required for access to the ELM suppression regime[17]. Because reduction of the RMP amplitude leads to an increased pressure pedestal height, this enables global confinement recovery in an ELM-free state[30] by adjusting RMP levels. To avoid ELMs while maximizing the confinement, we use a pre-programmed low $n = 1$ RMP spectrum[8] with 90 degree phasing and apply real-time feedback to control its amplitude. During the plasma current flattop before applying RMP, with $I_p = 0.51$ MA and $\sim$ 3 MW of co-neutral beam injection heating, $\beta_{\mathrm{N}} \sim 2.13$, $\beta_{\mathrm{p}} \sim 1.71$, and $H_{98} \sim 1.03$, close to the targets of the proposed ITER baseline scenario. In this discharge, the plasma edge safety factor $q_{95} \sim 5$, which is higher than the target value of $q_{95} \sim 3$. Here, q_{95} is defined as the pitch of the magnetic field line in the edge where the normalized poloidal flux (ψ_{N}) is 95%. However, after achieving the first stable ELM suppression through traditional means (7.1 s), the plasma performance significantly decreases to $\beta_{\mathrm{N}} \sim 1.62$, $\beta_{\mathrm{p}} \sim 1.30$, and $H_{98} \sim 0.68$. The 30% reduction in overall confinement by RMP mainly comes

from degradation in density and temperature pedestal, as shown in Fig.1c, d. Such extensive confinement and H_{98} degradation is a well-known general trend in low-n RMP experiments[31–33] and will not be acceptable in a future fusion reactor because this leads to a significant increase in fusion cost.

After this initial degradation, the real-time adaptive ELM control scheme starts to recover the original performance before RMPs were introduced while maintaining stable ELM suppression. The controller leverages the D_α emission signal near the outer divertor target to calculate the frequency of ELMs (f_{ELM})[34] in real-time and change I_{RMP} accordingly. To achieve ELM suppression, the RMP amplitude (or coil current, I_{RMP}) is raised until f_{ELM} decreases to 0, i.e., ELM suppression. Then, during the resulting ELM-free period, the controller lowers the RMP strength to raise the pedestal height until ELMs reappear, at which point the control again starts to ramp up the RMP amplitude until suppression is recovered (Fig.1a). In the experiment presented in Fig.1, there are 0.5 s of RMP flattop intervals between the RMP-ramp up and down phase to achieve saturated RMP response. Throughout this process, we adjust the lower bound of I_{RMP} to slightly higher value (by 0.1kA) than where the most recent ELM returns. This adaptive constraint reduces the likelihood of ELM suppression loss and control oscillation. The feedback system leads the plasma to a converged operating point that optimizes both ELM-free operation and confinement, recovering most of the performance lost in the initial application of RMP.

In the selected discharge, this adaptive ELM control scheme achieves a stable ELM-free phase at 10.5 s with recovered global confinement, as shown in Fig.1b. Although a few ELMs occur before convergence, the controller successfully reaches a stable operating point with minimized ELMy periods. In the final state, the plasma performance shows $\beta_{\mathrm{N}} \sim 1.91$, $\beta_{\mathrm{p}} \sim 1.53$, and $H_{98} \sim 0.9$, recovering up to 68% of the original confinement degradation. Such increase in H_{98} is especially important as this leads to the 60% recovery in Q_{fus} degradation, thus emphasizing the performance of adaptive control.

B. Recovery of pedestal height by adaptive RMP control

The enhanced confinement quality by adaptive RMP control occurs with the recovery of both the temperature and density pedestals. For the profile reconstruction, ion temperature is measured by charge exchange recombination system[35] for Carbon (6+) impurities at outboard mid-plane. Electron temperature is measured by the Thomson Scattering[36] and Electron Cyclotron emission[37]

system. Core electron density is measured by the Thomson Scattering and Two-color interferometry system[38]. To obtain well-resolved profiles, the data are averaged over 100 ms. The pedestal height is obtained from hyperbolic tangent fits with edge profiles, where its location depends on the pedestal width. The equilibria from EFIT code[39] is used for the radial profile mapping and fitting. Kinetic equilibria are reconstructed for the plasma detailed analysis. This equilibrium is calculated with the pressure profile (summation of thermal pressure profile from radial profile reconstruction and fast ion pressure from NUBEAM code[40]) and current density profile (core current from motional Stark effect diagnostics[41] and edge current using NUBEAM, Ohmic and Sauter current models[42]) as a constraint. Fig.1c and d shows the time traces of fitted pedestal heights for all channels. As can be seen in the figure, all pedestals are significantly improved from the first ELM suppression phase (7.1 s). For example, electron ($T_{\mathrm{e,ped}}$) and ion ($T_{\mathrm{i,ped}}$) temperature pedestals increase by 22% and 50%, respectively. In addition, the electron density pedestal ($n_{\mathrm{e,ped}}$) is also recovered by 10% at the same time. Interestingly, $H_{98} \sim 0.9$ at 10.5 s is much larger than $H_{98} \sim 0.75$ at 6.2 s, even with the same $I_{\mathrm{RMP}} = 3.6$ kA. This indicates that the confinement recovery by adaptive approach is not solely attributable to decreased I_{RMP}, but rather that another contributor leads the plasma to a reinforced recovery to the high-confinement state.

We note that the ion temperature pedestal exhibits significant recovery compared to the other channels. This is mainly due to the rapid and significant increase of ion temperature pedestal height by decreasing RMP strength. The traces of pedestal height versus I_{RMP} before the first ELM reappearance (5.3-7.7s) reveal this trend. Fig.2 shows the changes of ion, electron temperature and electron density with respect to the I_{RMP} during 5.3 s to 7.7 s. In the figure, $n_{\mathrm{e,ped}}$ and $T_{\mathrm{e,ped}}$ have a similar dependence on I_{RMP} during the pedestal degradation (5.3-6.5s) and recovery (7.1-7.7s) phases, showing $\frac{\Delta n_{\mathrm{e,ped}}}{\Delta I_{\mathrm{RMP}}} \sim -10^{15}/m^3\mathrm{A}$ and $\frac{\Delta T_{\mathrm{e,ped}}}{\Delta I_{\mathrm{RMP}}} \sim -0.06$ eV/A. However, $T_{\mathrm{i,ped}}$ in the recovery phase shows a 50% larger response of -0.09eV/A compared to the degradation phase, -0.06eV/A. The difference of responses in these phases leads to the faster and larger recovery of the ion temperature pedestal. Here, Fig.2d shows that β_{p} exhibits similar trend with $T_{\mathrm{i,ped}}$, where $\frac{\Delta \beta_{\mathrm{p}}}{\Delta I_{\mathrm{RMP}}}$ in the recovery phase has a 50% larger response of -0.14/kA compared to the degradation phase, -0.07/kA. Because such a boosted response of β_{p} leads to the reinforced confinement recovery, this similarities between $T_{\mathrm{i,ped}}$ and β_{p} responses indicates that $T_{\mathrm{i,ped}}$ dynamic can be considered as a key to the successful confinement optimization via adaptive RMP control.

In addition to the changes of pedestal heights, the radial profiles during discharges are compared. Fig.3 illustrates the radial profiles of ion, electron temperature, and density at three im-

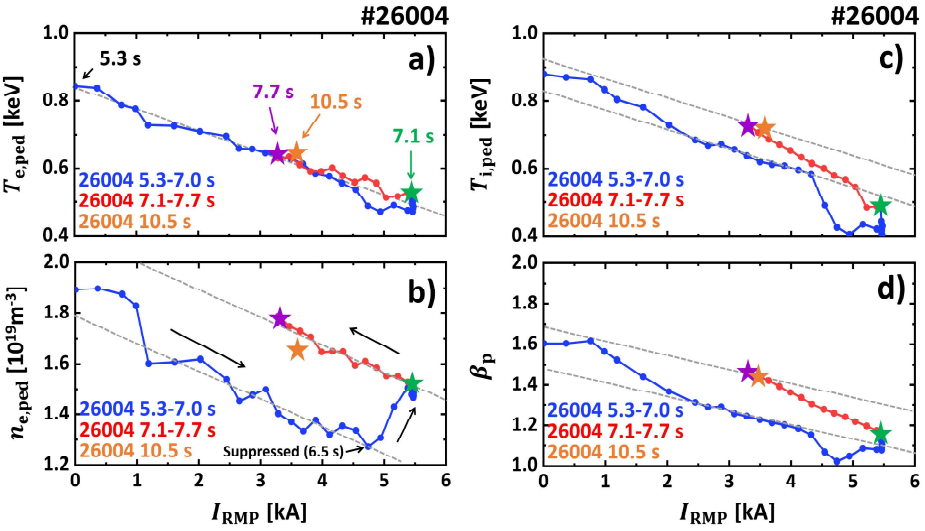

FIG. 2. Pedestal heights and global confinement for RMP ramp-up (5.3-7.1 s, blue), down (7.1-7.7 s, red), first saturated ELM-suppression (7.1 s, green), first optimized suppression (7.7 s, purple), and finally optimized suppression (10.5 s, orange). Pedestal height of **a** electron temperature $T_{e,ped}$, **b** electron density $n_{e,ped}$ and **c** ion temperature $T_{i,ped}$. **d** Global poloidal beta β_p. Ion temperature is measured by a charge-exchange recombination system for carbon (6+) impurities. Electron temperature is measured by the Thomson Scattering and Electron cyclotron emission system. Electron density is measured by the Thomson Scattering and Two-color interferometry system.

portant time slices during the recovery phase; first saturated ELM suppression state (7.1 s), first optimized ELM suppression state (7.7 s), and finally converged state (10.5 s). As shown in Fig.3a-c, all radial profiles in the core plasma are almost identical during the recovery phase. Therefore, the improved confinement by decreasing RMP strength results from increased $n_{e,ped}$, $T_{e,ped}$, and $T_{i,ped}$, with the last one dominant. Here, the statistical error bars of $n_{e,ped}$, $T_{e,ped}$, and $T_{i,ped}$ are $\sim 12\%$, $\sim 11\%$, and $\sim 5\%$, respectively. It turns out that $\sim 67\%$ of improvement comes from the ion temperature pedestal, while the contribution of $n_{e,ped}$ and $T_{e,ped}$ to the confinement recovery is 20% and 13% respectively. In this respect, the recovery of $T_{i,ped}$ is responsible for reinforced recovery by adaptive control. The large growth of $T_{i,ped}$ is mainly due to the simultaneously increased upper limit of $T_{i,ped}$ before the loss of ELM suppression and its enhanced response to the RMP strength. In addition, $n_{e,ped}$ shows a large increase near $I_{RMP} \sim 5$ kA (Fig.2b), which can be attributed to reduced particle pumping from ELMs. This occurs before 7 s and does not directly contribute to confinement recovery beginning at 7.1 s. However, it still strengthens the

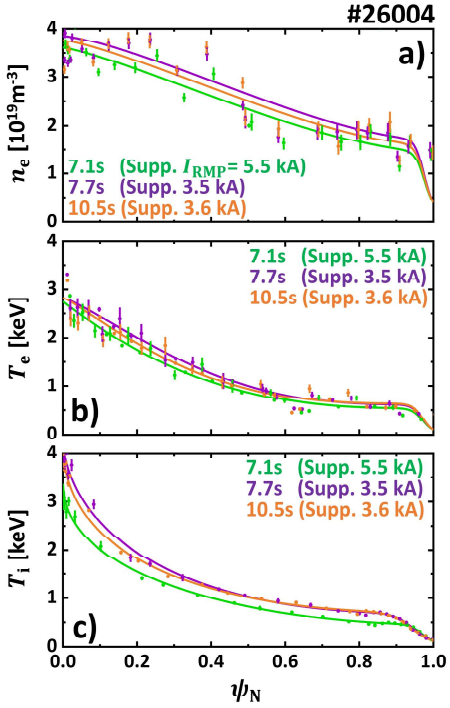

FIG. 3. Radial profiles for first saturated ELM-suppression (7.1 s, green), first optimized suppression (7.7 s, purple), and finally optimized suppression (10.5 s, orange). **a** Electron density, **b** electron temperature and **c** ion temperature with statistical error bars. Ion temperature is measured by a charge-exchange recombination system for carbon (6+) impurities. Electron temperature is measured by the Thomson Scattering and Electron cyclotron emission system. Electron density is measured by the Thomson Scattering and Two-color interferometry system.

confinement recovery with increasing $T_{i,ped}$. Given that the profiles of 7.7 s and 10.5 s are very similar, control iterations after 7.7 s can be considered as a repeated cycles similar to first ELM suppression period (5.3-7.7 s) for the control convergence. Therefore, the following analysis is focused on the first control iteration for easier explanation.

III. ACHIEVING SAFE ELM SUPPRESSION WITH ADAPTIVE CONTROL

In standard H-mode discharges, strong RMPs are favorable for entering the ELM suppression but also raises the possibility of dangerous plasma destabilization. Too large of an RMP field in the core plasma normally leads to a locking of plasma rotation and invokes a disastrous core insta-

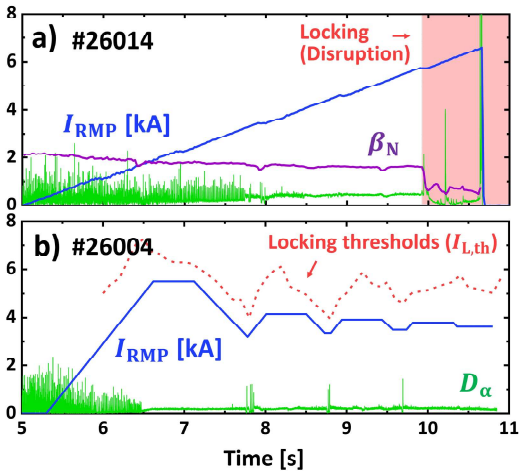

FIG. 4. Time traces of RMP-induced locking and suppression discharge with $n = 1$ RMP in KSTAR. **a** RMP coil current (blue), D_α emission (green), and β_N (purple) of discharge #26014. Onset of locking (disruption) is marked as a red region. **b** RMP coil current (blue) and D_α emission (green) of discharge #26004. The disruption thresholds in I_{RMP} is marked as a red dotted line.

bility called a disruption. Figure.4a. shows the adjacent discharge (#26014) whose RMP-induced locking occurs at 10 s with sudden drop of plasma confinement (β_N). This core locking (or disruptions) terminates the plasma and forms transient heat fluxes on the tokamak walls which are even more severe than ELMs. Unfortunately, plasma disruption is easier with low-n RMPs. Therefore it is vital to maintain the RMP strength between the thresholds of ELM suppression and disruption. To complicate this process, these thresholds change in time with various plasma parameters and are often hard to theoretically predict. The database[33] for $n = 1$ RMP ELM suppression in KSTAR reveals broadly scattered experimental thresholds showing $1 \sim 2$ kA variations, and empirical prediction is also challenging due to their sensitivity to plasma parameters. For these reasons, in the present experiments, a series of discharges are used to find safe RMP strength for ELM suppression. This approach will not be applicable in a fusion reactor, where a single disruption can result in the termination of machine life.

Notably, the adaptive approach lowers the RMP strength after entering the ELM-free state and maintains it near the levels for marginally stable ELM suppression. This automatically avoids touching the disruptive limits. Previous study[43] revealed that the locking occurs when perturbed field at core region ($\delta B_{r,core}$) exceeds the certain limit. This study calculates the perturbed radial fields (δB_r) by RMP using the ideal plasma response code, IPEC[44], with given magnetic equi-

libria and I_{RMP}. The core responses $\delta B_{\mathrm{r,core}}$ is derived off-line through radially averaging δB_{r} at $\psi_{\mathrm{N}} = 0-0.9$. Based on the calculated response, the empirical $\delta B_{\mathrm{r,core}}$ threshold for core-locking is obtained from neighboring discharge (#26014) as $\sim$ 26G. The predicted locking thresholds ($I_{\mathrm{L,th}}$) in I_{RMP} are equivalent to the δB_{r} thresholds based on the ideal plasma response calculation. As shown in Fig.4b, the RMP strength in the adaptive RMP discharge (#26004) stays safely below the $I_{\mathrm{L,th}}$ threshold throughout the example discharge, highlighting the advantages of this adaptive scheme for achieving stable ELM suppression. Here, the $I_{\mathrm{L,th}}$ exhibits similar trend with I_{RMP} because $\delta B_{\mathrm{r,core}}$ increases with β_{N} even with the same applied field strength. Although adaptive RMP control will be ineffective if only a small margin exists between the thresholds for suppression and disruption, it still reduces the necessity of extensive optimization of the RMP geometry for locking avoidance, which often comes at the expense of other important parameters or operational degrees of freedom.

IV. ION TEMPERATURE PEDESTAL BROADENING AND ADAPTIVE ELM CONTROL

A. Improved ELM stability and ion temperature pedestal response by ion-pedestal widening

As mentioned earlier, the RMP induces additional transport process in the edge region, resulting the degradation of pedestal height and its gradient. However, RMP-induced pedestal transport can also facilitate the improvement of the $T_{\mathrm{i,ped}}$ upper limit in the ELM-free phase and its response to the RMP strength by broadening the ion temperature pedestal. Effect of RMP-induced transport on the ion temperature pedestal can be found from the analysis of the profiles in detail. Fig.5a, b illustrate ion temperature pedestal and $E \times B$ flow (ω_{E})profiles for five times between 5.3 and 7.7 s. Before ELM suppression (5.3-6.3 s), $T_{\mathrm{i,ped}}$ decreases with I_{RMP}, while the pedestal gradient is well sustained (or even slightly increased). After ELM suppression (> 6.5 s), however, the pedestal gradient starts to change. The transition from 6.6 to 7.1 s shows broadening of the ion temperature pedestal and decreasing of its gradient. This widening is maintained in the pedestal recovery phase up to 7.7 s. The decrease in pedestal height and gradient are both due to RMP-induced transport. However, the rapid broadening of the ion temperature pedestal after ELM suppression indicates that its gradient is not governed by the transport affecting the pedestal height but instead by an

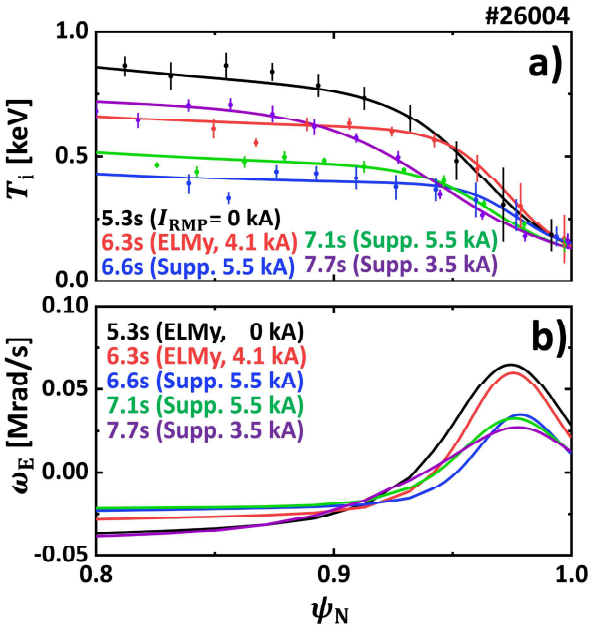

FIG. 5. Time traces of pedestal profiles during adaptive ELM control (#26004). **a** Ion temperature pedestal profiles with statistical error bars are shown for five different time slices. **b** ExB flow profiles (ω_E) at pedestal are shown for five different time slices.

"additional" transport source that occurs in the ELM suppression phase. For example, reduced ω_E profiles and its gradient with ion temperature pedestal broadening may indicate the change of turbulence and neoclassical transport, which is known to increase with smaller $E \times B$ well at the pedestal region[45,46].

The change in ion temperature pedestal width improves the ELM stability. In theory, pedestal pressure (P_{ped}) or pedestal poloidal beta ($\beta_{p,ped} = \frac{P_{ped}}{B_p^2/2\mu_0}$) should stay under the stability limit to avoid the reappearance of ELM crashes. Although it is not yet theoretically revealed how low $\beta_{p,ped}$ should be than this limit, the stability analysis confirms that experimental $\beta_{p,ped}$ stays below $\sim 70\%$ of the stability limit during the ELM suppression phase. Therefore, in this work, we assumes the ELM suppression can be maintained under the 70% of $\beta_{p,ped}$ limit imposed by stability constraint.Here, the pedestal stability is predicted using ideal peeling-ballooning (PBM) theory[3] and the EPED1[47] algorithm. The fixed-boundary equilibrium code, CHEASE[48], is used for accurate equilibrium mapping, and the ideal MHD stability code, MISHKA1[49], is employed for PBM stability calculation. All other required parameters are taken from the reconstructed radial profiles and plasma equilibrium.

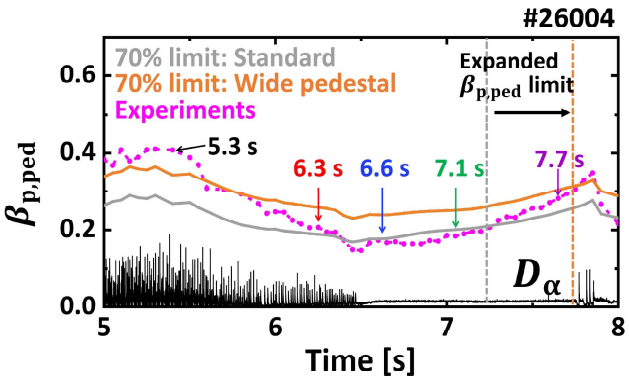

FIG. 6. Time traces of pedestal stability limits during adaptive ELM control (#26004). **a** Ion temperature pedestal profiles with statistical error bars are shown for five different time slices. 70% of ELM stability limit for $\beta_{p,ped}$ with (orange) and without (gray) wide ion temperature pedestal, calculated from EPED code. Experimentally measured $\beta_{p,ped}$ (magenta) and D_α emission (black) are also shown. The dotted lines show $\beta_{p,ped}$ limits during ELM-free state imposed by pedestal stability with (orange) and without (gray) wide ion temperature pedestal.

This stability limit is known to improve with increased pedestal width[50]. Therefore, widened pressure pedestal via ion-pedestal broadening allows for higher $\beta_{p,ped}$ during the ELM-free phase. Numerical analysis reveals that the $\beta_{p,ped}$ limit increases by 53% due to ion temperature pedestal broadening. This change is presented in Fig.6. In the figure, $\beta_{p,ped}$ limits derived with (orange) and without (gray) broadened ion temperature pedestal are presented with experimental points (magenta). It can be seen that the limit is enhanced by pedestal widening. With the expansion of the $\beta_{p,ped}$ limit illustrated as dotted lines, $\beta_{p,ped}$ can further increase from 0.2 (gray dotted line) to 0.31 (orange dotted line). This enhanced $\beta_{p,ped}$ limit allows access to higher $T_{i,ped}$ in the ELM suppression phase. For example, ELM suppression can be maintained at 7.7 s where $T_{i,ped}$=0.7 keV, which is higher than 0.6 keV in ELMy phase (6.3 s), as shown in Fig.2c.

The broader ion-pedestal also can lead to a larger response of $T_{i,ped}$ on RMP strength. Inspired from (Hu et al. 2020)[51], the change of temperature pedestal height (ΔT_{ped}) by ΔI_{RMP} and magnetic islands can be described as Eq.1,

$$\frac{\Delta T_{ped}}{\Delta I_{RMP}} \approx \nabla T_{ped} \sum_{m \geq q_{ped}} \frac{\partial W_{m,n}}{\partial I_{RMP}}, \tag{1}$$

where $W_{m,n}$ and ∇T_{ped} are the (m,n) island width and pedestal gradient, respectively. q_{ped} is the edge safety factor on the pedestal top. This expression is based on the concept where the

contribution of an island on the pedestal degradation (ΔT_{ped}) by RMP is the accumulation of profile flattening at the islands in the pedestal region. We note that constant ∇T_{ped} over the pedestal region is assumed to make interpretation easier. This expression addresses that pedestal height changes more rapidly with RMP strength as the pedestal gradient grows and q_{ped} decreases. With the given q profile monotonic, q_{ped} is reduced by increasing pedestal width. Because the summation term ($\sum ..$) increases with q_{ped} and width, the broadened ion temperature pedestal can lead to a stronger response of $T_{\mathrm{i,ped}}$ despite the decrease of ion temperature pedestal gradient (∇T_{ped}). In addition, ion temperature pedestal is known to be heavily influenced by neoclassical transport[15,46,52]. Here, RMP can increase the neoclassical heat flux and the amount is roughly proportional to the square of perturbed field strength and I^2_{RMP}. Smaller edge $E \times B$ can increase the sensitivity of ion heat flux to RMP strength[53,54]. Because a decreased ion temperature pedestal gradient reduces the ω_{E}[19,55] at the pedestal (Fig.5b), this change in radial electric field also contributes to increasing the response of $T_{\mathrm{i,ped}}$.

On the other hand, the responses of $n_{\mathrm{e,ped}}$ and $T_{\mathrm{e,ped}}$ to RMP strength are almost identical whether or not the ELMs are fully suppressed. This means that additional RMP-induced transport in the ELM-free phase has a smaller effect on the electron density and temperature pedestal gradient. Although the electron pedestal width has considerable uncertainty due to limitations in the resolution of edge diagnostics, its value lies between 4-6% in normalized poloidal flux without showing a considerable widening like ion temperature pedestal, suggesting that additional transport has only a relatively small effect on electron channels. We note that a large decrease in electron pedestal height still occurs without a clear change in its width, and this additional transport is expected to have little correlation with "pump-out" commonly observed in RMP experiments.

B. Advantages of wide ion temperature pedestal in adaptive ELM control.

Increased $T_{\mathrm{i,ped}}$ response by RMP-induced transport leads to an extensive recovery of $T_{\mathrm{i,ped}}$ during RMP ramp-down and makes an ion temperature pedestal higher than the RMP ramp-up phase (ELMy) even with the same RMP strength. In addition, enhanced pedestal stability allows for larger $T_{\mathrm{i,ped}}$ before the return of ELMs. The synergy between these effects boosts the pedestal recovery and enables adaptive control to maximize the confinement, resulting in a much higher

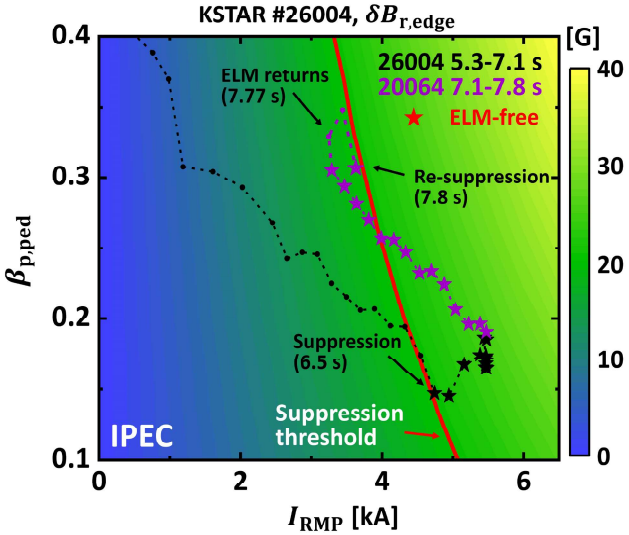

FIG. 7. The pressure pedestal height $\beta_{p,ped}$ versus RMP strength during adaptive ELM control (#26004). The time traces of $\beta_{p,ped}$ in #26004 discharge for 5.3-7.1 s (black) and 7.1-7.8 s (purple) with varying I_{RMP}. ELM-free states are marked as star dots. Contours of δB_r at pedestal region from ideal response calculation using IPEC are also shown. Experimentally derived $\delta B_{r,edge}$ threshold for ELM suppression is drawn as a red curve.

pedestal than during the initial phase of ELM suppression, as shown in Fig.7, which illustrates $\beta_{p,ped}$ versus I_{RMP}. The changes to the pedestal from 5.3 to 7.8 s are shown, and the ELM suppressed states are marked with star points.

Another advantage of RMP-induced transport is that it improves the control stability. Adaptive control can be unstable due to a bifurcation of the plasma state during transitions between ELMy and ELM-free regimes, which causes oscillation of the control system. In particular, it can take a long time or even become impossible for a controller to find the optimal solution because of the sudden jump in RMP strength required for re-entry (I_{IN}) to or exit (I_{OUT}) from ELM suppression. The schematic diagram in Fig.8a illustrates how this characteristic will delay the control convergence. In practice, ELM control must be done quickly to minimize damage to the reactor, so an adaptive approach is generally hard to use in such a bifurcating system. However, RMP-induced transport eases these control difficulties by reducing I_{IN} during adaptive control, as shown in Fig.8b.

It has been shown that the plasma enters the ELM suppression state above a certain $\delta B_{r,edge}$ threshold[43], where $\delta B_{r,edge}$ is the perturbed radial field strength at the pedestal. Again, $\delta B_{r,edge}$ is

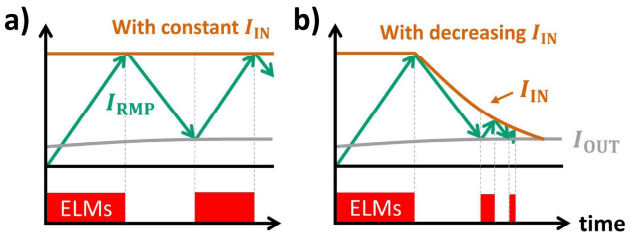

FIG. 8. Schematic diagram of adaptive ELM control using RMPs. Here, RMP threshold for ELM suppression entry (I_{IN}, orange) and exit (I_{OUT}, gray) are drawn. Time trace of I_{RMP} (green) and onset of ELMs (red box) are also shown. Expected time trace of adaptive ELM control with **a** constant I_{IN} and **b** decreasing I_{IN} in time.

calculated using IPEC code[44] and derived through radially averaging δB_{r} at $\psi_{\mathrm{N}} = 0.9 - 1.0$. The thresholds of δB_{r} for RMP-induced ELM suppression is obtained from the reference discharge (#26004). This threshold ($\sim$ 20 G) is shown as the red contour of Fig.7. Here, $\beta_{\mathrm{p,ped}}$ amplifies the perturbed field[43], and the same δB_{r} can be obtained with a smaller I_{RMP} with larger $\beta_{\mathrm{p,ped}}$. Because RMP-induced transport enhances $\beta_{\mathrm{p,ped}}$ in an ELM-free state, this leads to a lower I_{IN}, making access to the next ELM suppression regime easier. The ELM suppression of 7.8 s shown in Fig.7 results from reduced I_{IN} compared to the former one at 6.5 s. Thus, I_{IN} for each suppression entry changes as $4.9 \rightarrow 3.6 \rightarrow 3.53 \rightarrow 3.5$ kA, as seen in Fig.1(a), resulting in fast and stable system optimization. This interesting example shows uncommon *positive effect*[56,57] of self-organized transport on pedestal confinement.

We note that such an RMP-induced hysteresis shown in Fig7 is not trivial to be produced in the experiment as it conventionally requires a delicate pre-programmed RMP waveform under the absence of real-time control. This leads to difficulties in investigating and exploiting the hysteresis, which is critical to optimize the ELM-free state. In this respect, adaptive RMP control is an effective methodology as it can automatically generate the hysteresis and utilize it. In addition, the adaptive scheme has been successfully operated for more than a hundred confinement times ($\sim$ 5 s) of KSTAR, and therefore, this control is also expected to be applicable to long pulse plasma in ITER.

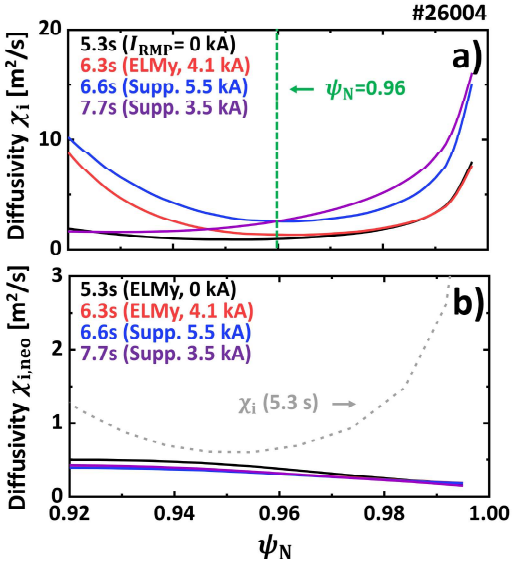

FIG. 9. The radial profiles of **a** experimental ion heat diffusivity (χ_i) and **b** theoretical ion neoclassical heat diffusivity ($\chi_{i,neo}$) for four different time slices including 5.3, 6.3, 6.6, and 7.7 s. Dotted gray line in **b** shows the radial χ_i profile at 5.3 s.

C. The RMP-induced transport and broadened ion-pedestal

It is worth pointing out that successful adaptive control in these experiments is mainly due to a broadened ion temperature pedestal during the ELM suppression phase. In order to determine the change in ion heat transport, interpretive transport analysis is conducted using ASTRA 7[58] code. The ion neoclassical heat diffusivity ($\chi_{i,neo}$) is also calculated based on NCLASS[53] model to compare it with experimental ion heat diffusivity (χ_i). The results are shown in Fig.9, where χ_i (a) and $\chi_{i,neo}$ (b) for 5.3-7.7 s are included. As shown in Fig.9a, the ion heat diffusivity (χ_i) of the pedestal region rapidly increases via additional transport after transitions to the ELM-free state. In addition, the pedestal heat diffusivity does not change much during 7.1-7.7 s, indicating that it is insensitive to the decreasing I_{RMP}. It has been reported that the neoclassical transport effect dominates ion heat transport under RMPs[46,52]. However, this collisional transport strongly depends on the RMP strength. Therefore, the broadened ion temperature pedestal does not seem to be related to the neoclassical process. Here, it can be seen in Fig.9b that χ_i at 5.3 s (gray) exceeds neoclassical level in all cases, supporting the existence of additional transport. We note that following analyses will focus on the center region of the pedestal ($\psi_N = 0.96$), where the change in ion heat diffusivity is clearly observed in time.

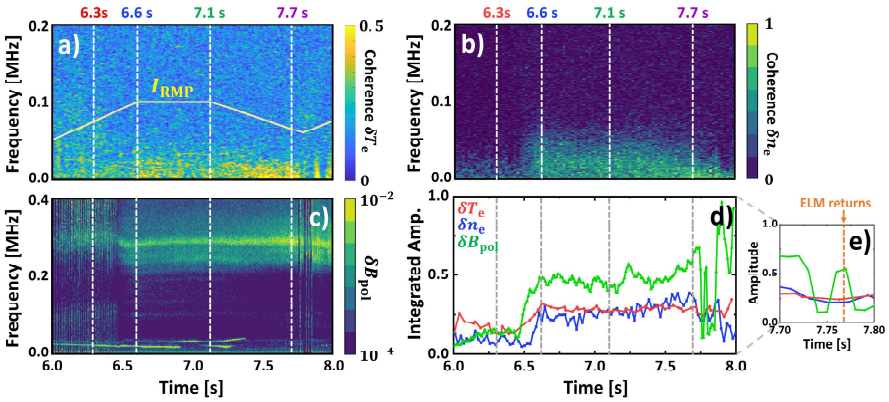

FIG. 10. A measured edge fluctuations during ELM-suppression state. **a** Coherence of edge T_e fluctuation from Electron cyclotron emission imaging system. **b** Coherence of edge n_e fluctuation from Beam emission imaging system. **c** Measured δB_{pol} fluctuation at inner wall from Mirnov coil. **d** Time trace of normalized integrated coherence amplitude of T_e (red), n_e (blue), and B_{pol} (green) fluctuations over the frequency space. **e** Zoom-in of **d** for $7.7-7.8$ s. The normalized RMP coil current I_{RMP} is illustrated in **a**.

Fluctuation measurements on KSTAR reveal significant edge turbulence triggered by RMPs[25,26,59] after ELM suppression. Fig.10a, b illustrate the spectrogram and the coherence strength of δT_e and δn_e fluctuations at $\psi_N \sim 0.96$. Fig.10c shows the poloidal magnetic field fluctuations (δB_{pol}) at the inner wall. In this work, edge T_e and n_e fluctuations ($k_y \rho_s \leqslant 0.3$) are measured from electron emission image spectroscopy (ECEI)[60] and beam emission spectroscopy (BES)[61], respectively. The k_y is the bi-normal wave number, $\rho_s = \sqrt{2m_i T_e}/eB$ is the hybrid Larmor radius, and m_i is deuterium mass. Magnetic field perturbations are captured by the Mirnov coil signal (MC)[62]. The spectrogram of the measured fluctuation is derived using the Fourier transform. Coherence of the electron density and temperature fluctuation is calculated from a bi-spectrum analysis with two radially adjacent channels in ECEI and BES, respectively. The ELM peaks and core modes are statistically removed from the integrated amplitude of coherent fluctuations in all channels. Here, δT_e and δn_e have strong coherence over the frequency range of 10-70 kHz. The magnetic fluctuations in the 200-400 kHz range are also observed during the same period. As shown in Fig.10d, they show an immediate instigation of turbulence as ELM suppression begins followed by quick saturation within 200 ms. We note that coherence before 6.4 s comes from ELM noise, and a magnetic signal of <50 kHz is due to core modes. It is noteworthy that the strength of coherent fluctuations remains almost identical during 6.6-7.7 s. Here, the widening of the ion temperature pedestal coincides with the occurrence of edge fluctuations. Furthermore, they are both insensitive

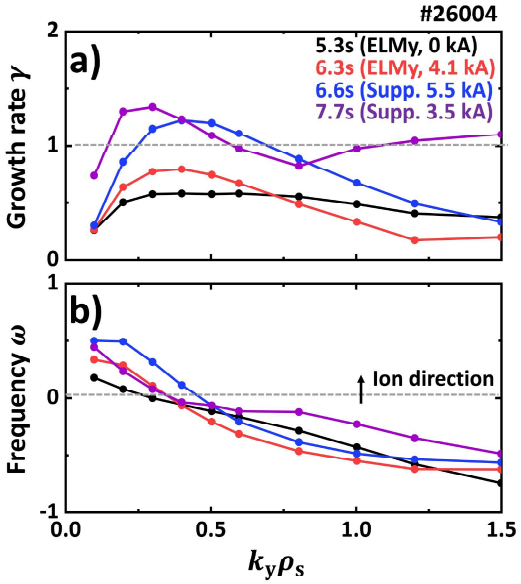

FIG. 11. The **a** normalized growth rates **b** and real frequency of instability calculated from CGYRO for four different time slices including 5.3, 6.3, 6.6, and 7.7 s.

to RMP strength. Therefore, these similarities support the claim that the ion temperature pedestal is widened primarily due to increased heat diffusivity by edge turbulence.

Linear gyrokinetic simulations confirms that enhanced edge turbulence may occur in the ELM suppression phase. The gyrokinetic code, CGYRO[63], is used in the linear analysis of micro-instabilities. The linear initial value solver is employed to find the unstable mode in the target radial point with wavelength $k_y\rho_s = 0.1 - 1.5$. This simulation is based on a flux-tube approach with a full gyro-kinetic description for both electron and ion channels. The reconstructed radial profiles and kinetic equilibrium described above are included for the accurate modeling. This calculation is performed at $\psi_N = 0.96$, where the changes of experimental fluctuations are robust. The linear growth rate and real frequency are normalized by $E \times B$ shearing rate (γ_E) and Bohm sound speed (C_S).

As shown in Fig.11a, the normalized linear growth rates (γ) of turbulence mode exceed the onset limit (>1) after the transitions to the ELM-free state. This is mainly due to decreased stabilizing effect from the ExB shearing rate (γ_E)[45,64], which comes from the degraded pressure pedestal (Fig.5b) after entering ELM suppression (6.6 s). The real frequency and numerical testing indicates that the excited mode is an ITG/TEM hybrid mode, which mainly lies on ion direction as shown in Fig.11b. Here, the bi-normal wave length $k_y\rho_s \sim 0.3$ and real frequency ~ 51 kHz of

the most unstable mode exhibits similar properties to the measured fluctuations of electron channels. The simulation results show that ion thermal diffusion can be increased with these unstable modes, supporting the idea of ion temperature pedestal broadening by turbulence. However, theoretical analysis on RMP-induced turbulence still has many missing pieces. Recent studies have shown that the characteristics of transport in the presence of RMP deviates significantly from linear gyrokinetic calculations, raising the importance of non-linearity[65] and non-locality[66] which is not included in this linear analysis. In addition, the reduced gradient of ion temperature pedestal during its broadening can be explained by introducing RMP-induced transport. However, it is still less clear how it can contribute to increased width. In the future, nonlinear gyrokinetic studies including these aspects will shed further light on the accurate description of edge turbulence under RMPs.

The considerable effect of RMP-induced transport on ion heat diffusion might be inconsistent with the general trend of other devices[16,17,32], where such turbulence mainly affects electron channel and has a minor effect on ion transport. Although it is difficult to evaluate the turbulence effect on n_e and T_e due to limitations in the diagnostics, we still confirm that there is a clear correlation between edge fluctuation and ion temperature pedestal. Therefore, this observation suggests new possible role of turbulence in the ion temperature pedestal, where ELM-free state is achieved with the low-n($= 1$) RMP.

As discussed earlier, ion temperature pedestal widening is key to the fast and successful convergence of adaptive control. Because edge-turbulence can play important role on the ion-pedestal, the turbulence level should be well sustained to maintain such an favorable effect. However, Fig.10d shows that the amplitude of edge fluctuation disappears as ELMs re-occur, and the favorable effects from widened ion temperature pedestal will also start to decrease. Here, the ion temperature pedestal will return to its initial ELMy state on an energy confinement time scale, so the advantageous turbulence effect can last a few hundred ms after returning to the ELMy phase. Thus, I_{RMP} must re-increase immediately after the loss of ELM suppression fully exploit this effect. In this respect, a real-time adaptive ELM control is a unique methodology both to utilize and control the edge turbulence and to uncover the novel beneficial effect of turbulence.

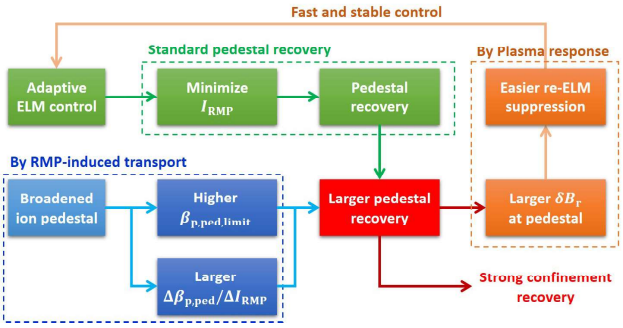

FIG. 12. Schematic diagram of correlation between adaptive ELM control and pedestal recovery. Here, it is noteworthy that the strong recovery of confinement is also attributable to the widened ion temperature pedestal by RMP-induced transport during ELM suppression phase.

V. CONCLUSION

We have achieved successful optimization of a controlled ELM-free state with highly recovered confinement by $\sim 60\%$, maintaining $\beta_N \sim 1.91$, $\beta_p \sim 1.53$, and $H_{98} \sim 0.9$, with the original degradation in fusion gain largely recovered. This novel adaptive approach exhibits compatibility between RMP ELM suppression and high confinement. In addition, it provides a reliable strategy to achieve stable ELM-free access by preventing RMP-induced disruption. It is noteworthy that the remarkable recovery of confinement is not solely attributable to adaptive RMP control but also to a widened ion temperature pedestal resulting from RMP-induced transport that promotes pedestal recovery by improving the ion response and ELM stability and facilitates fast, stable, and reinforced control optimization (Fig.12). This feature, which can be correlated to the turbulent process, is a good example of a system that transitions to an optimal state through a self-organized response to adaptive modulation. These results with low $n = 1$ RMP confirm that adaptive ELM control is a highly promising approach towards optimizing the ELM-free state, potentially solving one of the most challenging obstacles for viable and economical fusion energy.

However, there are remaining features to be improved for a "complete" adaptive ELM control picture. As shown in Fig.1a, the current approach is based on ELM detection and thereby inevitably faces several ELMs during control. This limitation could be critical at the reactor level, where a single ELM can already be dangerous. Thus, a way to detect the loss of ELM suppression in advance of the ELM re-occurrence is needed. Here, the behavior of edge turbulence suggests a potential solution. The amplitude of magnetic fluctuation during the ELM-free phase shows a

rapid decrease 50 ms before the return of ELMs at 7.77 s (Fig.10e). Such an abrupt change in magnetic signals is an effective indicator of suppression loss and has been also observed in other device[25]. Therefore, this property could be potentially utilized in real-time to entirely avoid the return of ELM to achieve truly ELM-free optimization. Future work will focus on developing its detection schemes.

Previous work has shown that the effectiveness of RMP ELM suppression can be enhanced by physics model-based 3D geometric optimization[67]. Since this adaptive ELM control scheme maximizes the plasma performance for a given scenario, any additional improvements from external forces will be augmented by the adaptive scheme. This makes the adaptive approach a prime candidate to fully exploit existing physics models for RMP ELM suppression.

Lastly, the demonstration of adaptive control in this work is limited to 11 s. Although the control convergence is likely to be achieved before 10.5 s, it is still important to check its validity and reproducibility in a longer pulse for its application in ITER. In addition, RMPs up to $n = 5$ will be utilized in ITER operation, so adaptive ELM control using higher n (> 1) RMP also needs to be verified. Future investigation of these features will lead to broader operational freedom and higher confinement recovery, as well as the development of advanced ELM control techniques for ITER and future tokamaks.

VI. ACKNOWLEDGMENTS

The authors would like to thank the KSTAR team. This material was supported by the U.S. Department of Energy, under Awards DE-SC0020372. This research was also supported by R&D Program of "KSTAR Experimental Collaboration and Fusion Plasma Research(EN2021-12)" through the Korea Institute of Fusion Energy(KFE) funded by the Government funds.

REFERENCES

[1]F. Wagner, G. Fussmann, T. Grave, M. Keilhacker, M. Kornherr, K. Lackner, K. McCormick, E. R. Müller, A. Stäbler, G. Becker, K. Bernhardi, U. Ditte, A. Eberhagen, O. Gehre, J. Gernhardt, G. v. Gierke, E. Glock, O. Gruber, G. Haas, M. Hesse, G. Janeschitz, F. Karger, S. Kissel, O. Klüber, G. Lisitano, H. M. Mayer, D. Meisel, V. Mertens, H. Murmann, W. Poschenrieder, H. Rapp, H. Röhr, F. Ryter, F. Schneider, G. Siller, P. Smeulders, F. Söldner, E. Speth, K. H.

Steuer, Z. Szymanski, and O. Vollmer, en"Development of an Edge Transport Barrier at the H-Mode Transition of ASDEX," Physical Review Letters **53**, 1453–1456 (1984).

[2]A. Sips, J. Schweinzer, T. Luce, S. Wolfe, H. Urano, J. Hobirk, S. Ide, E. Joffrin, C. Kessel, S. Kim, P. Lomas, I. Nunes, T. Pütterich, F. Rimini, W. Solomon, J. Stober, F. Turco, P. de Vries, JET Contributors, The ASDEX Upgrade team, The DIII-D team, The C-Mod team, The JT-60U team, and ITPA-IOS TG members and experts, en"Assessment of the baseline scenario at q_{95} ~ 3 for ITER," Nuclear Fusion **58**, 126010 (2018).

[3]J. W. Connor, R. J. Hastie, H. R. Wilson, and R. L. Miller, en"Magnetohydrodynamic stability of tokamak edge plasmas," Physics of Plasmas **5**, 2687–2700 (1998).

[4]A. Loarte, G. Huijsmans, S. Futatani, L. Baylor, T. Evans, D. M. Orlov, O. Schmitz, M. Becoulet, P. Cahyna, Y. Gribov, A. Kavin, A. Sashala Naik, D. Campbell, T. Casper, E. Daly, H. Frerichs, A. Kischner, R. Laengner, S. Lisgo, R. Pitts, G. Saibene, and A. Wingen, en"Progress on the application of ELM control schemes to ITER scenarios from the non-active phase to DT operation," Nuclear Fusion **54**, 033007 (2014).

[5]J. Gunn, S. Carpentier-Chouchana, F. Escourbiac, T. Hirai, S. Panayotis, R. Pitts, Y. Corre, R. Dejarnac, M. Firdaouss, M. Kočan, M. Komm, A. Kukushkin, P. Languille, M. Missirlian, W. Zhao, and G. Zhong, en"Surface heat loads on the ITER divertor vertical targets," Nuclear Fusion **57**, 046025 (2017).

[6]T. E. Evans, R. A. Moyer, P. R. Thomas, J. G. Watkins, T. H. Osborne, J. A. Boedo, E. J. Doyle, M. E. Fenstermacher, K. H. Finken, R. J. Groebner, M. Groth, J. H. Harris, R. J. L. Haye, C. J. Lasnier, S. Masuzaki, N. Ohyabu, D. G. Pretty, T. L. Rhodes, H. Reimerdes, D. L. Rudakov, M. J. Schaffer, G. Wang, and L. Zeng, "Suppression of Large Edge-Localized Modes in High-Confinement DIII-D Plasmas with a Stochastic Magnetic Boundary," Physical Review Letters **92** (2004), 10.1103/physrevlett.92.235003, publisher: American Physical Society (APS).

[7]W. Suttrop, T. Eich, J. C. Fuchs, S. Günter, A. Janzer, A. Herrmann, A. Kallenbach, P. T. Lang, T. Lunt, M. Maraschek, R. M. McDermott, A. Mlynek, T. Pütterich, M. Rott, T. Vierle, E. Wolfrum, Q. Yu, I. Zammuto, and H. Zohm, en"First Observation of Edge Localized Modes Mitigation with Resonant and Nonresonant Magnetic Perturbations in ASDEX Upgrade," Physical Review Letters **106**, 225004 (2011).

[8]Y. M. Jeon, J.-K. Park, S. W. Yoon, W. H. Ko, S. G. Lee, K. D. Lee, G. S. Yun, Y. U. Nam, W. C. Kim, J.-G. Kwak, K. S. Lee, H. K. Kim, and H. L. Yang, "Suppression of Edge Localized Modes in High-Confinement KSTAR Plasmas by Nonaxisymmetric Magnetic Perturbations," Physical

Review Letters **109** (2012), 10.1103/physrevlett.109.035004, publisher: American Physical Society (APS).

[9]Y. Sun, Y. Liang, Y. \. e. Liu, S. Gu, X. Yang, W. Guo, T. Shi, M. Jia, L. Wang, B. Lyu, C. Zhou, A. Liu, Q. Zang, H. Liu, N. Chu, H. \. e. Wang, T. Zhang, J. Qian, L. Xu, K. He, D. Chen, B. Shen, X. Gong, X. Ji, S. Wang, M. Qi, Y. Song, Q. Yuan, Z. Sheng, G. Gao, P. Fu, and B. Wan, "Nonlinear Transition from Mitigation to Suppression of the Edge Localized Mode with Resonant Magnetic Perturbations in the EAST Tokamak," Physical Review Letters **117** (2016), 10.1103/physrevlett.117.115001, publisher: American Physical Society (APS).

[10]M. E. Fenstermacher, T. E. Evans, T. H. Osborne, M. J. Schaffer, M. P. Aldan, J. S. deGrassie, P. Gohil, I. Joseph, R. A. Moyer, P. B. Snyder, R. J. Groebner, M. Jakubowski, A. W. Leonard, O. Schmitz, and the DIII-D Team, en"Effect of island overlap on edge localized mode suppression by resonant magnetic perturbations in DIII-D," Physics of Plasmas **15**, 056122 (2008).

[11]F. L. Waelbroeck, I. Joseph, E. Nardon, M. Bécoulet, and R. Fitzpatrick, "Role of singular layers in the plasma response to resonant magnetic perturbations," Nuclear Fusion **52**, 074004 (2012), publisher: IOP Publishing.

[12]Q. M. Hu, R. Nazikian, B. A. Grierson, N. C. Logan, J.-K. Park, C. Paz-Soldan, and Q. Yu, "The density dependence of edge-localized-mode suppression and pump-out by resonant magnetic perturbations in the DIII-D tokamak," Physics of Plasmas **26**, 120702 (2019), publisher: AIP Publishing.

[13]R. Fitzpatrick, "Theory of edge localized mode suppression by static resonant magnetic perturbations in the DIII-D tokamak," Physics of Plasmas **27**, 042506 (2020), publisher: AIP Publishing.

[14]Y. Liu, C. Paz-Soldan, L. Li, and Y. Sun, en"Role of 3D neoclassical particle flux in density pump-out during ELM control by RMP in DIII-D," Nuclear Fusion **60**, 036018 (2020).

[15]V. Rozhansky, P. Molchanov, E. Kaveeva, S. Voskoboynikov, A. Kirk, E. Nardon, D. Coster, and M. Tendler, en"Modelling of the edge plasma of MAST in the presence of resonant magnetic perturbations," Nuclear Fusion **51**, 083009 (2011).

[16]S. Mordijck, R. A. Moyer, and G. R. McKee, en"Changes in density fluctuations as a result of resonant magnetic perturbations correlate with the density inverse scale length," Physics of Plasmas **19**, 024504 (2012).

[17]G. McKee, Z. Yan, C. Holland, R. Buttery, T. Evans, R. Moyer, S. Mordijck, R. Nazikian, T. Rhodes, O. Schmitz, and M. Wade, en"Increase of turbulence and transport with resonant

magnetic perturbations in ELM-suppressed plasmas on DIII-D," Nuclear Fusion **53**, 113011 (2013).

[18]H. Müller, T. Lunt, W. Suttrop, T. Eich, R. Fischer, J. Fuchs, A. Herrmann, M. Kočan, P. de Marné, and E. Wolfrum, en"Modification of scrape-off layer transport and turbulence by non-axisymmetric magnetic perturbations in ASDEX Upgrade," Journal of Nuclear Materials **438**, S64–S71 (2013).

[19]N. Vianello, C. Rea, M. Agostini, R. Cavazzana, G. Ciaccio, G. De Masi, E. Martines, A. Mazzi, B. Momo, G. Spizzo, P. Scarin, M. Spolaore, P. Zanca, M. Zuin, L. Carraro, P. Innocente, L. Marrelli, M. E. Puiatti, and D. Terranova, en"Magnetic perturbations as a viable tool for edge turbulence modification," Plasma Physics and Controlled Fusion **57**, 014027 (2015).

[20]C. Rea, N. Vianello, M. Agostini, R. Cavazzana, G. De Masi, E. Martines, B. Momo, P. Scarin, S. Spagnolo, G. Spizzo, M. Spolaore, and M. Zuin, en"Comparative studies of electrostatic turbulence induced transport in presence of resonant magnetic perturbations in RFX-mod," Nuclear Fusion **55**, 113021 (2015).

[21]L. Cui, R. Nazikian, B. Grierson, E. Belli, T. Evans, N. Logan, D. Orlov, S. Smith, G. Staebler, and P. Snyder, en"The energy confinement response of DIII-D plasmas to resonant magnetic perturbations," Nuclear Fusion **57**, 116030 (2017).

[22]S. Liu, N. Yan, Y. Liang, H. Zhang, J. Xu, G. Xu, L. Wang, R. Chen, G. Hu, Y. Ye, Y. Sun, T. Shi, H. Wang, M. Wu, X. Wu, S. Gu, M. Jia, N. Chu, Q. Ma, Y. Wang, T. Zhang, X. Han, L. Chen, J. Liu, S. Xu, H. Wang, N. Zhao, W. Zhang, J. Qian, L. Zeng, L. Xu, S. Wang, H. Liu, Q. Zang, Y. Yu, L. Liao, X. Gong, and EAST, en"Edge turbulence characteristics and transport during the ELM mitigation with $n = 1$ resonant magnetic perturbation on EAST," Nuclear Fusion **60**, 082001 (2020).

[23]M. W. Jakubowski, T. E. Evans, M. E. Fenstermacher, M. Groth, C. J. Lasnier, A. W. Leonard, O. Schmitz, J. G. Watkins, T. Eich, W. Fundamenski, R. A. Moyer, R. C. Wolf, L. B. Baylor, J. A. Boedo, K. H. Burrell, H. Frerichs, J. S. deGrassie, P. Gohil, I. Joseph, S. Mordijck, M. Lehnen, C. C. Petty, R. I. Pinsker, D. Reiter, T. L. Rhodes, U. Samm, M. J. Schaffer, P. B. Snyder, H. Stoschus, T. Osborne, B. Unterberg, E. Unterberg, and W. P. West, "Overview of the results on divertor heat loads in RMP controlled H-mode plasmas on DIII-D," Nuclear Fusion **49**, 095013 (2009), publisher: IOP Publishing.

[24]P. Snyder, K. Burrell, H. Wilson, M. Chu, M. Fenstermacher, A. Leonard, R. Moyer, T. Osborne, M. Umansky, W. West, and X. Xu, en"Stability and dynamics of the edge pedestal in the low

collisionality regime: physics mechanisms for steady-state ELM-free operation," Nuclear Fusion **47**, 961–968 (2007).

[25]R. Nazikian, C. Paz-Soldan, J. \. e. Callen, J. \. e. deGrassie, D. Eldon, T. \. e. Evans, N. \. e. Ferraro, B. \. e. Grierson, R. \. e. Groebner, S. \. e. Haskey, C. \. e. Hegna, J. \. e. King, N. \. e. Logan, G. \. e. McKee, R. \. e. Moyer, M. Okabayashi, D. \. e. Orlov, T. \. e. Osborne, J.-K. Park, T. \. e. Rhodes, M. \. e. Shafer, P. \. e. Snyder, W. \. e. Solomon, E. \. e. Strait, and M. \. e. Wade, "Pedestal Bifurcation and Resonant Field Penetration at the Threshold of Edge-Localized Mode Suppression in the DIII-D Tokamak," Physical Review Letters **114** (2015), 10.1103/physrevlett.114.105002, publisher: American Physical Society (APS).

[26]C. Paz-Soldan, R. Nazikian, S. \. e. Haskey, N. \. e. Logan, E. \. e. Strait, N. \. e. Ferraro, J. \. e. Hanson, J. \. e. King, M. \. e. Lanctot, R. \. e. Moyer, M. Okabayashi, J.-K. Park, M. \. e. Shafer, and B. \. e. Tobias, "Observation of a Multimode Plasma Response and its Relationship to Density Pumpout and Edge-Localized Mode Suppression," Physical Review Letters **114** (2015), 10.1103/physrevlett.114.105001, publisher: American Physical Society (APS).

[27]G. Lee, J. Kim, S. Hwang, C. Chang, H. Chang, M. Cho, B. Choi, K. Kim, K. Cho, S. Cho, K. Choh, C. Choi, J. Choi, J. Choi, I. Choi, C. Do, T. Ha, J. Han, J. Hong, K. Hong, N. Hur, I. Hwang, K. Im, H. Jhang, Y. Jung, B. Kim, D. Kim, G. Kim, H. Kim, J. Kim, J. Kim, W. Kim, Y. Kim, K. Kwon, M. Kyum, B. Lee, D. Lee, H. Lee, J. Lee, S. Lee, H. Na, Y. Oh, J. Park, H. Ri, Y. Ryoo, K. Song, H. Yang, J. Yang, B. Yoo, S. Yoo, N. Yoon, S. Yoon, G. You, K. You, W. Choe, D.-I. Choi, S. Jeong, D. Lee, Y. Bae, H. Kang, G. Kim, I. Ko, W. Namkung, J. Oh, Y. Bae, Y. Cho, B. Hong, G. Hong, C. Hwang, S. In, M. Ju, H. Lee, B. Oh, B. Yoon, S. Baang, H. Choi, J. Hwang, M. Kim, Y. Kim, S. Lee, J. Yee, C. Yoon, K.-H. Chung, S. Hong, Y. Hwang, S. Kim, Y. Kim, K. Chung, J. Lim, D. Ha, S. Oh, K. Ryu, Q. Wang, T. Ko, J. Joo, S. Suh, C. Choi, J. Lee, Y. Lee, H. Shin, I. Song, J. Baek, I. Han, Y. Koh, P. Park, C. Ryu, J. Cho, D. Hwang, Y. Kim, J. Schmidt, H. Park, G. Neilson, W. Reiersen, R. Simmons, S. Bernabei, F. Dahlgren, L. Grisham, S. Jardin, C. Kessel, J. Manickam, S. Medley, N. Pomphrey, J. Sinnis, T. Brown, R. White, K. Young, J. Schultz, P. Wang, L. Sevier, M. Carter, P. Ryan, D. Swain, D. Hill, W. Nevins, and B. Braams, en"The KSTAR project: An advanced steady state superconducting tokamak experiment," Nuclear Fusion **40**, 575–582 (2000).

[28]I. P. E. G. o. C. Transport, I. P. E. G. o. C. Database, and I. P. B. Editors, "Chapter 2: Plasma confinement and transport," Nuclear Fusion **39**, 2175–2249 (1999).

[29]H. Zohm, en"On the Minimum Size of DEMO," Fusion Science and Technology **58**, 613–624 (2010).

[30]F. Laggner, D. Eldon, A. Nelson, C. Paz-Soldan, A. Bortolon, T. Evans, M. Fenstermacher, B. Grierson, Q. Hu, D. Humphreys, A. Hyatt, R. Nazikian, O. Meneghini, P. Snyder, E. Unterberg, E. Kolemen, and t. DIII-D team, en"Real-time pedestal optimization and ELM control with 3D fields and gas flows on DIII-D," Nuclear Fusion **60**, 076004 (2020).

[31]Y. In, J.-K. Park, Y. M. Jeon, J. Kim, G. Y. Park, J.-W. Ahn, A. Loarte, W. H. Ko, H. H. Lee, J. W. Yoo, J. W. Juhn, S. W. Yoon, and H. P. and, "Enhanced understanding of non-axisymmetric intrinsic and controlled field impacts in tokamaks," Nuclear Fusion **57**, 116054 (2017), publisher: IOP Publishing.

[32]C. Sung, G. Wang, T. L. Rhodes, S. P. Smith, T. H. Osborne, M. Ono, G. R. McKee, Z. Yan, R. J. Groebner, E. M. Davis, L. Zeng, W. A. Peebles, and T. E. Evans, en"Increased electron temperature turbulence during suppression of edge localized mode by resonant magnetic perturbations in the DIII-D tokamak," Physics of Plasmas **24**, 112305 (2017).

[33]M. Kim, J. Lee, W. H. Ko, S.-H. Hahn, Y. In, Y. M. Jeon, W. Suttrop, S. K. Kim, G. Y. Park, J.-W. Juhn, and J. H. Lee, en"Pedestal electron collisionality and toroidal rotation during ELM-crash suppression phase under $n = 1$ RMP in KSTAR," Physics of Plasmas **27**, 112501 (2020).

[34]D. Eldon, E. Kolemen, J. Barton, A. Briesemeister, D. Humphreys, A. Leonard, R. Maingi, M. Makowski, A. McLean, A. Moser, and P. Stangeby, en"Controlling marginally detached divertor plasmas," Nuclear Fusion **57**, 066039 (2017).

[35]Won-Ha Ko, Seungtae Oh, and Myeun Kwon, en"KSTAR Charge Exchange Spectroscopy System," IEEE Transactions on Plasma Science **38**, 996–1000 (2010).

[36]J. H. Lee, S. Oh, H. M. Wi, W. R. Lee, K. P. Kim, K. team, I. Yamada, K. Narihara, and K. Kawahata, en"Tangential Thomson scattering diagnostic for the KSTAR tokamak," Journal of Instrumentation **7**, C02026–C02026 (2012).

[37]G. S. Yun, W. Lee, M. J. Choi, J. B. Kim, H. K. Park, C. W. Domier, B. Tobias, T. Liang, X. Kong, N. C. Luhmann, and A. J. H. Donné, en"Development of KSTAR ECE imaging system for measurement of temperature fluctuations and edge density fluctuations," Review of Scientific Instruments **81**, 10D930 (2010).

[38]K. Lee, J.-W. Juhn, Y. Nam, Y. Kim, H. Wi, S. Kim, and Y.-c. Ghim, en"The design of two color interferometer system for the 3-dimensional analysis of plasma density evolution on KSTAR," Fusion Engineering and Design **113**, 87–91 (2016).

[39]L. Lao, H. St. John, R. Stambaugh, A. Kellman, and W. Pfeiffer, en"Reconstruction of current profile parameters and plasma shapes in tokamaks," Nuclear Fusion **25**, 1611–1622 (1985).

[40]A. Pankin, D. McCune, R. Andre, G. Bateman, and A. Kritz, en"The tokamak Monte Carlo fast ion module NUBEAM in the National Transport Code Collaboration library," Computer Physics Communications **159**, 157–184 (2004).

[41]J. Chung, J. Ko, J. Howard, C. Michael, G. v. Nessi, A. Thorman, and M. F. M. D. Bock, "Motional Stark effect diagnostics for KSTAR," Journal of the Korean Physical Society **65**, 1257–1260 (2014), publisher: Korean Physical Society.

[42]O. Sauter, C. Angioni, and Y. R. Lin-Liu, en"Neoclassical conductivity and bootstrap current formulas for general axisymmetric equilibria and arbitrary collisionality regime," Physics of Plasmas **6**, 2834–2839 (1999).

[43]J.-K. Park, Y. Jeon, Y. In, J.-W. Ahn, R. Nazikian, G. Park, J. Kim, H. Lee, W. Ko, H.-S. Kim, N. C. Logan, Z. Wang, E. A. Feibush, J. E. Menard, and M. C. Zarnstroff, "3D field phase-space control in tokamak plasmas," Nature Physics **14**, 1223–1228 (2018), publisher: Springer Science and Business Media LLC.

[44]J.-k. Park, A. H. Boozer, and A. H. Glasser, en"Computation of three-dimensional tokamak and spherical torus equilibria," Physics of Plasmas **14**, 052110 (2007).

[45]H. Biglari, P. H. Diamond, and P. W. Terry, "Influence of sheared poloidal rotation on edge turbulence," Physics of Fluids B: Plasma Physics **2**, 1–4 (1990), publisher: AIP Publishing.

[46]V. Rozhansky, E. Kaveeva, P. Molchanov, I. Veselova, S. Voskoboynikov, D. Coster, A. Kirk, S. Lisgo, and E. Nardon, en"Modification of the edge transport barrier by resonant magnetic perturbations," Nuclear Fusion **50**, 034005 (2010).

[47]P. B. Snyder, R. J. Groebner, A. W. Leonard, T. H. Osborne, and H. R. Wilson, en"Development and validation of a predictive model for the pedestal height," Physics of Plasmas **16**, 056118 (2009).

[48]H. Lütjens, A. Bondeson, and O. Sauter, "The CHEASE code for toroidal MHD equilibria," Computer Physics Communications **97**, 219–260 (1996), publisher: Elsevier BV.

[49]A. Mikhailovskii, G. Huysmans, W. Kerner, and S. Sharapov, "Optimization of computational MHD normal-mode analysis for tokamaks," Plasma Physics Reports **23**, 844–857 (1997).

[50]T. Osborne, G. Jackson, Z. Yan, R. Maingi, D. Mansfield, B. Grierson, C. Chrobak, A. McLean, S. Allen, D. Battaglia, A. Briesemeister, M. Fenstermacher, G. McKee, P. Snyder, and The DIII-D Team, "Enhanced H-mode pedestals with lithium injection in DIII-D," Nuclear Fusion

55, 063018 (2015).

[51]Q. Hu, R. Nazikian, B. Grierson, N. Logan, D. Orlov, C. Paz-Soldan, and Q. Yu, en"Wide Operational Windows of Edge-Localized Mode Suppression by Resonant Magnetic Perturbations in the DIII-D Tokamak," Physical Review Letters **125**, 045001 (2020).

[52]E. Viezzer, M. Cavedon, P. Cano-Megias, E. Fable, E. Wolfrum, D. J. Cruz-Zabala, P. David, R. Dux, R. Fischer, G. F. Harrer, F. M. Laggner, R. M. McDermott, U. Plank, T. Pütterich, M. Willensdorfer, and the ASDEX Upgrade Team, en"Dynamics of the pedestal transport during edge localized mode cycles at ASDEX Upgrade," Plasma Physics and Controlled Fusion **62**, 024009 (2020).

[53]W. A. Houlberg, K. C. Shaing, S. P. Hirshman, and M. C. Zarnstorff, en"Bootstrap current and neoclassical transport in tokamaks of arbitrary collisionality and aspect ratio," Physics of Plasmas **4**, 3230–3242 (1997).

[54]S. Mordijck, R. Moyer, N. Ferraro, M. Wade, and T. Osborne, en"The radial electric field as a measure for field penetration of resonant magnetic perturbations," Nuclear Fusion **54**, 082003 (2014).

[55]J. Lee, Y. M. Jeon, Y. In, G. Y. Park, G. S. Yun, W. Lee, M. Kim, J. H. Lee, W. H. Ko, and H. K. P. and, "Direct evidence of E × B flow changes at the onset of resonant magnetic perturbation-driven edge-localized mode crash suppression," Nuclear Fusion **59**, 066033 (2019), publisher: IOP Publishing.

[56]X. Chen, K. Burrell, T. Osborne, W. Solomon, K. Barada, A. Garofalo, R. Groebner, N. Luhmann, G. McKee, C. Muscatello, M. Ono, C. Petty, M. Porkolab, T. Rhodes, J. Rost, P. Snyder, G. Staebler, B. Tobias, Z. Yan, and the DIII-D Team, en"Stationary QH-mode plasmas with high and wide pedestal at low rotation on DIII-D," Nuclear Fusion **57**, 022007 (2017).

[57]R. Nazikian, C. Petty, A. Bortolon, X. Chen, D. Eldon, T. Evans, B. Grierson, N. Ferraro, S. Haskey, M. Knolker, C. Lasnier, N. Logan, R. Moyer, D. Orlov, T. Osborne, C. Paz-Soldan, F. Turco, H. Wang, and D. Weisberg, en"Grassy-ELM regime with edge resonant magnetic perturbations in fully noninductive plasmas in the DIII-D tokamak," Nuclear Fusion **58**, 106010 (2018).

[58]G. V. Pereverzev and P. N. Yushmanov, en"ASTRA Automated System for TRansport Analysis," , 147.

[59]J. Lee, G. S. Yun, M. J. Choi, J.-M. Kwon, Y.-M. Jeon, W. Lee, N. C. Luhmann, and H. K. Park, "Nonlinear Interaction of Edge-Localized Modes and Turbulent Eddies in Toroidal

Plasma undern=1Magnetic Perturbation," Physical Review Letters **117** (2016), 10.1103/physrevlett.117.075001, publisher: American Physical Society (APS).

[60]G. S. Yun, W. Lee, M. J. Choi, J. Lee, M. Kim, J. Leem, Y. Nam, G. H. Choe, H. K. Park, H. Park, D. S. Woo, K. W. Kim, C. W. Domier, N. C. Luhmann, N. Ito, A. Mase, and S. G. Lee, "Quasi 3D ECE imaging system for study of MHD instabilities in KSTAR," Review of Scientific Instruments **85**, 11D820 (2014), publisher: AIP Publishing.

[61]Y. U. Nam, S. Zoletnik, M. Lampert, Kovácsik, and H. M. Wi, en"Edge electron density profiles and fluctuations measured by two-dimensional beam emission spectroscopy in the KSTAR," Review of Scientific Instruments **85**, 11E434 (2014).

[62]J. G. Bak, S. G. Lee, D. Son, and the KSTAR Project Team, en"Performance of the magnetic sensor and the integrator for the KSTAR magnetic diagnostics," Review of Scientific Instruments **75**, 4305–4307 (2004).

[63]J. Candy, E. Belli, and R. Bravenec, en"A high-accuracy Eulerian gyrokinetic solver for collisional plasmas," Journal of Computational Physics **324**, 73–93 (2016).

[64]T. S. Hahm and K. H. Burrell, "Flow shear induced fluctuation suppression in finite aspect ratio shaped tokamak plasma," Physics of Plasmas **2**, 1648–1651 (1995), publisher: AIP Publishing.

[65]R. Hager, C. S. Chang, N. M. Ferraro, and R. Nazikian, en"Gyrokinetic understanding of the edge pedestal transport driven by resonant magnetic perturbations in a realistic divertor geometry," Physics of Plasmas **27**, 062301 (2020), arXiv: 2003.07130.

[66]S. Taimourzadeh, L. Shi, Z. Lin, R. Nazikian, I. Holod, and D. Spong, en"Effects of RMP-induced changes of radial electric fields on microturbulence in DIII-D pedestal top," Nuclear Fusion **59**, 046005 (2019).

[67]S. Yang, J.-K. Park, N. Logan, C. Zhu, Q. Hu, Y. Jeon, Y. In, W. Ko, S. Kim, Y. Lee, and Y. Na, "Localizing resonant magnetic perturbations for edge localized mode control in KSTAR," Nuclear Fusion **60**, 096023 (2020).